Physics in Medicine &
Biology

IPEM
Institute of Physics and Engineering in Medicine

PAPER • **OPEN ACCESS**

GPU-accelerated Monte Carlo simulation of electron and photon interactions for radiotherapy applications

To cite this article: G Franciosini *et al* 2023 *Phys. Med. Biol.* **68** 044001

View the article online for updates and enhancements.

You may also like

- FRED: a fast Monte Carlo code on GPU for quality control in Particle Therapy
M De Simoni, M Fischetti, E Gioscio et al.
- The Peculiar Precursor of a Gamma-Ray Burst from a Binary Merger Involving a Magnetar
Shuo Xiao, Yan-Qiu Zhang, Zi-Pei Zhu et al.
- NICER Discovery that SRGA J144459.2−604207 Is an Accreting Millisecond X-Ray Pulsar
Mason Ng, Paul S. Ray, Andrea Sanna et al.

This content was downloaded from IP address 151.100.44.95 on 07/03/2025 at 11:19

IOP Publishing Phys. Med. Biol. 68 (2023) 044001 https://doi.org/10.1088/1361-6560/aca1f2

Physics in Medicine & Biology

IPEM Institute of Physics and Engineering in Medicine

OPEN ACCESS

RECEIVED
15 June 2022

REVISED
20 October 2022

ACCEPTED FOR PUBLICATION
10 November 2022

PUBLISHED
15 February 2023

Original content from this work may be used under the terms of the Creative Commons Attribution 4.0 licence.

Any further distribution of this work must maintain attribution to the author(s) and the title of the work, journal citation and DOI.

PAPER

GPU-accelerated Monte Carlo simulation of electron and photon interactions for radiotherapy applications

G Franciosini[1,2], G Battistoni[3], A Cerqua[4], A De Gregorio[1,2], P De Maria[5], M De Simoni[1,2], Y Dong[3], M Fischetti[4], M Marafini[1,6], R Mirabelli[1,2], A Muscato[1,5], V Patera[1,4], F Salvati[4], A Sarti[1,4], A Sciubba[4,7], M Toppi[1,4], G Traini[1], A Trigilio[1,2] and A Schiavi[1,4]

[1] Istituto Nazionale di Fisica Nucleare (INFN) - Sezione di Roma, Italy
[2] Dipartimento di Fisica, Sapienza Università di Roma, Roma, Italy
[3] Istituto Nazionale di Fisica Nucleare (INFN) - Sezione di Milano, Italy
[4] Dipartimento di Scienze di Base e Applicate per Ingegneria, Sapienza Università di Roma, Roma, Italy
[5] Scuola post-laurea in Fisica Medica, Dipartimento di Scienze e Biotecnologie medico-chirurgiche, Sapienza Universitá di Roma, Roma, Italy
[6] Museo Storico della Fisica e Centro Studi e Ricerche 'E. Fermi', Roma, Italy
[7] Istituto Nazionale di Fisica Nucleare (INFN)- Laboratori Nazionali di Frascati, Frascati, Italy

E-mail: giacomo.traini@roma1.infn.it

Keywords: radiotherapy, Monte Carlo, GPU, treatment planning system, IORT, VHEE

Abstract

Objective. The Monte Carlo simulation software is a valuable tool in radiation therapy, in particular to achieve the needed accuracy in the dose evaluation for the treatment plans optimisation. The current challenge in this field is the time reduction to open the way to many clinical applications for which the computational time is an issue. In this manuscript we present an innovative GPU-accelerated Monte Carlo software for dose valuation in electron and photon based radiotherapy, developed as an update of the FRED (Fast paRticle thErapy Dose evaluator) software. *Approach*. The code transports particles through a 3D voxel grid, while scoring their energy deposition along their trajectory. The models of electromagnetic interactions in the energy region between 1 MeV—1 GeV available in literature have been implemented to efficiently run on GPUs, allowing to combine a fast tracking while keeping high accuracy in dose assessment. The FRED software has been bench-marked against state-of-art full MC (FLUKA, GEANT4) in the realm of two different radiotherapy applications: Intra-Operative Radio Therapy and Very High Electron Energy radiotherapy applications. *Results*. The single pencil beam dose-depth profiles in water as well as the dose map computed on non-homogeneous phantom agree with full-MCs at 2% level, observing a gain in processing time from 200 to 5000. *Significance*. Such performance allows for computing a plan with electron beams in few minutes with an accuracy of ∼%, demonstrating the FRED potential to be adopted for fast plan re-calculation in photon or electron radiotherapy applications.

1. Introduction

In radiotherapy the Treatment Planning System (TPS) is a complex software used to optimize the beam characteristics so as to provide the optimal dose delivery to the patient. Most of the commercial TPS provided by the machine vendors are based on analytical algorithms, which operate converting the patient morphology obtained from diagnostic examinations (e.g. CT, PET-CT or MRI scans) into electronic density in case of photon treatment, or into water-equivalent-path-length geometry in Particle Therapy (PT) with ion beams. However, this approach may fail to provide the necessary accuracy in presence of large density gradients (Paganetti 2009, Grassberger *et al* 2014, Liang *et al* 2020). On the other hand, general purpose Monte Carlo software as FLUKA (Ferrari *et al* 2005, Battistoni *et al* 2016) and GEANT4 (Agostinelli *et al* 2003, Allison *et al* 2016) are not suitable to be adopted in clinical routine due to their long computation time, and are mostly used only for treatment

© 2023 The Author(s). Published on behalf of Institute of Physics and Engineering in Medicine by IOP Publishing Ltd

recalculation in very complex cases. To overcome CPU time limitation typical of such accurate simulation tools, dose-engines running on graphics processing units (GPU) have been developed to combine the accuracy of Monte Carlo with the speed of analytical TPS, exploiting for a rapid particle transport the high parallel computing power allowed by GPU architecture. Today most of such implementations are designed for photon and particle therapy applications, as (Men *et al* 2009, Jia *et al* 2014, Wan Chan Tseung *et al* 2015, Tian *et al* 2015, Schiavi *et al* 2017, Mein *et al* 2018, Karbalaee *et al* 2020), that report software packages capable of evaluating a treatment plan in a few minutes.

Recently, the interest of using Very High Energy Electron beams (VHEE, i.e having a kinetic energy $>$50 MeV) for the treatment of deep-seated tumors was increased, also due to the observation of the FLASH sparing effect induced by high dose-rate beams ($\simeq$50–100 Gy/s). FLASH effect has been observed using electron, photon and proton beams (Favaudon *et al* 2014, Diffenderfer *et al* 2020, Montay-Gruel *et al* 2021, Ronga *et al* 2021), but the use of electron beams seems to represent the most viable and cost-effective solution to FLASH therapy clinical applications due to the recent improvement of the electron LINAC technology (Faillace *et al* 2021).

This new landscape induced in turn a new interest in fast MC codes for electron and photon transport (Wang *et al* 2016). In particular, GPU based MC platform dedicated to radiotherapy can have a large use, in particular in view of comparative studies of photon, electron and hadron based treatments.

In this manuscript we present a new GPU-accelerated dose-engine for electron and photon based radiotherapy applications, suitable for plan recalculation spanning from the energy scale of Intra-Operative electron Radio Therapy IOeRT ($\sim$5–10 MeV) up to that of VHEE radiotherapy ($\sim$100 MeV). The software core is shared with FRED (Fast paRticle thErapy Dose evaluator) (Schiavi *et al* 2017) software, developed for proton therapy, and recently extended for Carbon ion transport (De Simoni *et al* 2022). FRED is a proprietary software, adopted in several medical and research centers as a quality assurance tool for proton therapy. The details of our implementation are described in section 2, while the obtained time performance and accuracy in dose evaluation expected in VHEE radiotherapy application as well as in IORT are discussed in section 3.

2. Code structure and physical models

The FRED code structure is the same as that already implemented for hadron tracking. The front-end interface is written in C++, allowing to setup the simulation environment (CT importing, beam energy and direction), while the tracking kernel is coded using the CUDA toolkit (NVIDIA,Vingelmann and Fitzek 2020).

FRED architecture foresees a first initialisation stage operated on CPU, where the simulation environment is defined (grid size and dimension, material definition, treatment plan details) and the main physical quantities and properties needed for particle transport are pre-computed and stored in the GPU *texture* units. The particle tracking is fully operated by GPU, adopting a history-based approach in which each particle history is followed by a single GPU thread. Tracks are generated step-by-step using a class II MC algorithm (Berger 1963), i.e. the physical processes acting on the particle are divided into condensed-history or continuous models, and point-like or discrete interaction models. The stepping procedure is thoroughly described in (Schiavi *et al* 2017). The random engine used for sampling belongs to the KISS family proposed by (Marsaglia and Zaman 2006), which combines a multiply-with-carry generator, a Xorshift generator and a linear congruential generator. As it is an intrinsically serial algorithm, each GPU thread operates with its own generator. Two memory buffers shared between CPU and GPU are used to store the kinematic status of primary particles and to stack the generated secondary particles during the transport. The full FRED operation flow is summarised in figure 1.

Parallelisation of an MC tracking code on a GPU needs to take into account the hardware solutions adopted in high performance GPUs. In order to maximize the card occupancy, the number of registers per core has to be kept as low as possible. Whenever possible and accurate, a look-up table should be preferred to an analytical evaluation, e.g. in cross-section calculations. Access to memory locations, e.g. for scoring the dose on a 3D grid, has to be serialized using atomic operations to avoid data racing conditions among thousands of concurrent threads. Since many cores are sharing the same floating point units, calculations in double precision are costly in terms of performance, and therefore single precision has to be used wherever possible. We followed all these strategy hints in the re-implementation of the physics interaction models described in the following in order to maximise the tracking rate on the GPU.

At the energy scale of interest for electron-based radiotherapy applications (1–100 MeV) electrons travelling in matter lose energy by elastic collision with atomic electrons, exciting the internal atomic levels or producing ionisation electrons (delta-rays), as well as via the emission of Bremsstralhung radiation. When the emitted photons overcome the pair production threshold, an *electromagnetic shower* takes place, giving rise to a mixed field of electrons, positrons and photons. The amount of secondary particles emitted along the primary electron path affects in a significant way the total transport computation time. Tracking time heavily depends on primary

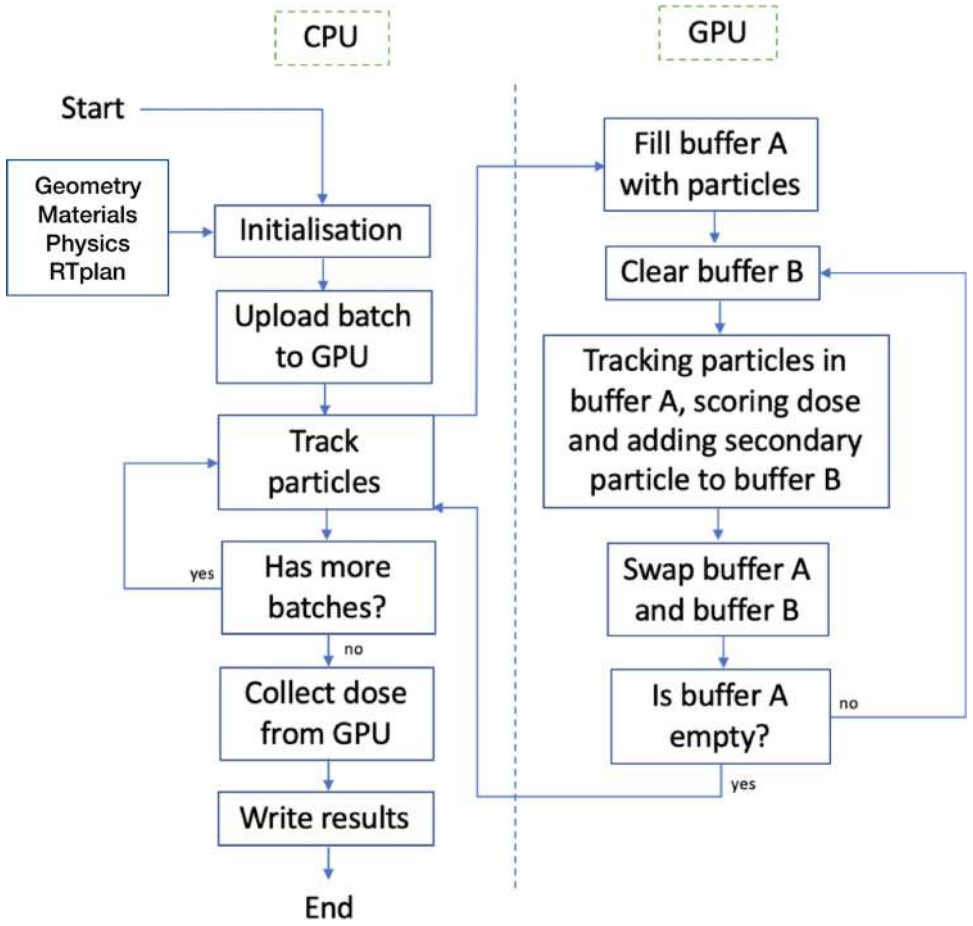

Figure 1. Sketch of the FRED architecture, in which the operation on charge of CPu and GPU are distinguished.

electron energy and on the chosen production and transport thresholds, that have to be finely tuned to match the accuracy/speed requested for each specific application.

In electron and positron transport the average energy loss $\overline{\Delta E}$ within a step due to electronic collisions under the delta-ray production threshold T_δ is treated as a continuous process as well as the angular deflection due to the Multiple Coulomb Scattering. All the other processes (Möller/Bhabha scattering, Bremsstrahlung, annihilation) are managed as discrete interactions, occurring when the particle has traveled for a path of length ds, which is random sampled according to an exponential distribution resulting in a mean free path in the material λ.

In photon tracking a point-like interaction (photoelectric absorption, Compton scattering, pair production, Rayleigh scattering) occurs at the end of a straight track according to dynamically calculated mass attenuation coefficients for each process. To balance accuracy and computation time, FRED relies on a set of look-up tables (LUT) in which most of the information and parameters needed for particle transport and process simulation are stored at the initialisation stage. Such approach is very efficient on GPU, which are equipped with *texture* units, a dedicated hardware for fast linear interpolation.

2.1. Continuous processes

2.1.1. Mean energy loss

Below the chosen delta-ray production threshold T_δ, the energy loss due to ejection of soft electrons is described by the restricted stopping power $\left(\frac{dE}{dx}\right)_{\text{res}}$, which is computed starting from the unrestricted stopping power provided by the NIST database (National Institute of Standards and Technology 2001), and subtracting the mean energy transferred to delta-rays per unit length according to

$$\left(\frac{dE}{dx}\right)_{\text{res}} = \left(\frac{dE}{dx}\right)_{\text{unres}} - \int_{T_\delta}^{T_{\max}} T \, \frac{d\sigma_\delta}{dT} \, dT \tag{1}$$

where $\frac{d\sigma_\delta}{dT}$ is the differential cross-section of the Möller and Bhabha scattering (described in 2.2.1). The unrestricted positron stopping power is obtained re-scaling that of electrons using the correction factors

reported in (Berger and Seltzer 1982) to take into account the different physical features of Moeller/Bhabha scattering.

The restricted stopping power from 10 keV to 1 GeV is stored in log-scaled look-up tables for several materials taken from NIST, and interpolated at each step using the Runge-Kutta RK4 method (Butcher 1996).

2.1.2. Energy straggling

The energy loss fluctuations are partially taken into account by generating delta-rays beyond the threshold T_δ in a discrete process. The residual statistical fluctuations which affect the continuous energy loss within a single step are computed using the model implemented in (GEANT4-Collaboration 2016). Depending on the κ value, which represents the lower limit of the number of collisions of the particle in a step ($\kappa = 10$ as default value) two different models are used. For mean energy loss $\overline{\Delta E} > = \kappa\ T_\delta$ in a step of length x we use a Gaussian distribution with variance σ^2 equal to:

$$\sigma^2 = 2\pi r_e^2 m_e c^2 N_{el} \frac{Z^2}{\beta^2} T_\delta x \left(1 - \frac{\beta^2}{2}\right) \tag{2}$$

where r_e is the classical electron radius, m_e is the electron rest mass, N_{el} is the electron density of the medium, Z is the charge of the incident particle and β is the relativistic velocity. In the other cases, i.e. $\overline{\Delta E} < \kappa T_\delta$, it is assumed that the atom involved in the collision has only two energy levels with binding energies E_1 and E_2, whose values are a function of the material. The particle-atom interaction in a given material can be an excitation with energy loss E_1 or E_2, or ionisation with energy loss distributed according to distribution $g(E) \sim 1/E^2$. The energy straggling is determined by the fluctuation of number of excitation and ionisation along the path. Under such assumptions, the average number of excitation $\bar{n}_1$, $\bar{n}_2$ at energies E_1, E_2 and the number of ionisation $\bar{n}_{ion}$ provoked by an electron which has released an amount of energy dE in a step of length dx are obtained as in (GEANT4-Collaboration 2016).

In the FRED implementation, a matrix for $\bar{n}_1$, $\bar{n}_2$ and $\bar{n}_{ion}$ is pre-calculated as a function of the incoming electron kinetic energy, the step length and material. For each step, the actual number of excitation n_1, n_2 and ionisation n_{ion} is sampled from a Poisson distribution having mean value corresponding to the interpolated values of $\bar{n}_1$, $\bar{n}_2$ and $\bar{n}_{ion}$. Thus, the energy loss in a step is formed by two separate contributions representing the energy loss due to excitation and ionisation respectively:

$$\Delta E = \Delta E_{exc} + \Delta E_{ion} \tag{3}$$

The excitation contribution to the energy loss is computed as

$$\Delta E_{exc} = n_1 E_1 + n_2 E_2 \tag{4}$$

while the ionisation contribution ΔE_{ion} can by obtained sampling n_{ion} times the $g(E)$ distribution using the inverse transform method:

$$\Delta E_{ion}(n_{ion},\ T_{th}) = \sum_{i=0}^{n_{ion}} \frac{E_0}{1 - u \cdot \frac{T_{th} - E_0}{T_{th}}} \tag{5}$$

where $E_0 = 10$ eV, u is randomly sampled between 0 and 1, and T_{th} is the production and transport kinetic energy threshold for electrons, positrons and photons. To speed-up the sampling process, the inverse cumulative distributions of the distributions $\Delta E_{ion}(n_{ion}, T_{Th})$ are pre-calculated and stored in a LUT during the FRED initialisation. In such way, the sampling at runtime requires only one table interpolation.

2.1.3. Multiple scattering

The angular deflection due to the multiple scattering interactions within the electron/positron step is sampled using the model proposed by (Al-Beteri and Raeside 1988) to parametrize the Moliere distribution: a gaussian term for small scattering angles, a modified relativistic Mott scattering term for large angle scattering, and an exponential term for intermediate angles. The probability of an electron being scattered by an angle between θ and $\theta + d\theta$ with respect to the incoming direction, when crossing a material with thickness t (expressed in g/cm^2) is given by:

$$2\pi f(\theta)d\theta = \begin{cases} \frac{2\theta}{WW_c}e^{-\frac{\theta^2}{W_c^2}}d\theta & 0 < \theta < W_c \\ \frac{2\theta P_1}{WW_c}e^{-\frac{P_2\theta}{W_c^2}}d\theta & \frac{3}{2}W_c < \theta < 3W_c \\ \frac{2W^2}{B\theta^3}\left(1+\frac{\pi W}{\theta}\right)d\theta & 3W_c < \theta < \pi \end{cases} \quad (6)$$

The parameter B is defined by the transcendental equation $b = B - ln(B)$, where b has the physical meaning of number of collisions inside the material and is computed using:

$$b = \ln\left(\frac{6680t(Z+1)Z^{\frac{1}{3}}}{\beta^2 A(1+3.34\Gamma^2)}\right) \quad (7)$$

P_1 and P_2 are determined requiring function continuity, while the characteristic angles W and W_c derive directly from the Moliere theory, being a function of the material and of the electron kinetic energy T as shown in the following equations:

$$W = X_c B^{\frac{1}{2}} \quad (8)$$

$$W_c = X_c(B - F(Z-t))^{\frac{1}{2}} \quad (9)$$

$$X_c = 4\pi r_e^2 N_A t \frac{Z(Z+1)}{A}\left(\frac{T+1}{T(T+2)}\right)^2 \quad (10)$$

$$F(Z,t) = 1.52Z^{0.46}t^{0.66} \quad (11)$$

In the FRED implementation, X_c, B, $F(Z, t)$ are precomputed and stored in LUTs for every defined material, as a function of the kinetic energy and material thickness. These parameters are linearly interpolated at run-time when evaluating the angular deviation in a step.

2.2. Discrete processes

The discrete processes are characterized by short-range interactions where the original particles ceases to exist or undergoes large variations in energy and/or direction. For electrons and positrons, the implemented discrete interactions are Bremsstrahlung emission and Möller/Bhabha scattering; for photons photoelectric effect, coherent (Rayleigh) and incoherent (Compton) scattering and pair production. The algorithm's core structure which manages the discrete interactions occurrence is detailed elsewhere (Schiavi *et al* 2017). To minimize the simulation time, most of the total cross sections of each process have been tabulated in the energy range of 1keV to 1 GeV for target elements with an atomic number ranging from 1 to 100. The electron and positron Bremsstrahlung total cross sections, as an example, have been calculated starting from the cross section differential tables, that provided the needed information as a function of the energy of the emitted photons energy, reported by Seltzer and Berger (Seltzer and Berger 1985). The total cross sections of the individual photon processes have been downloaded from the NIST XCOM Photons Cross sections Database (National Institute of Standards and Technology 2001). The Möller and Bhabha scattering total cross sections are instead analytically computed at initialisation for the needed materials and particles. In the appendix a detailed table of the used sources and LUTs is reported.

In the following sections, the implementation of aforementioned discrete processes is explained in detail.

2.2.1. Möller and Bhabha scattering

Above an energy threshold T_δ, a fraction of the electron and positron energy loss (about ~10%) is simulated by the explicit production of delta rays through the Möller ($e^-e^- \rightarrow e^-e^-$) and Bhabha ($e^+e^- \rightarrow e^+e^-$) scattering interactions. In our model T_δ is equal to 2 T_{th} and T_{th} for the electron and positron interaction respectively, where T_{th} is the production and transport energy cutoff which can be set by the user.

The probability of ejecting a delta-ray with a kinetic energy $E_\delta = \varepsilon E$ due to Möller and Bhabha scattering is written as in (GEANT4-Collaboration 2016).

$$\frac{d\sigma_{Moller}}{d\varepsilon} = \frac{2\pi r_e^2 Z}{\beta^2(\gamma-1)}\left[\frac{(\gamma-1)^2}{\gamma^2} + \frac{1}{\varepsilon}\left(\frac{1}{\varepsilon} - \frac{2\gamma-1}{\gamma^2}\right) + \frac{1}{1-\varepsilon}\left(\frac{1}{1-\varepsilon} - \frac{2\gamma-1}{\gamma^2}\right)\right] \quad (12)$$

$$\frac{d\sigma_{Bhabha}}{d\varepsilon} = \frac{2\pi r_e^2 Z}{(\gamma-1)}\left[\frac{1}{\beta^2\varepsilon^2} - \frac{2-y^2}{\varepsilon} + (1-2y)(3+y^2) - \right. \\ \left. + \varepsilon((1-2y)^2 + (1-2y)^3) + \varepsilon^2(1-2y)^3\right] \quad (13)$$

where ε is the fraction of transferred energy, $\gamma = E/m_e c^2$, β is the relativistic velocity, r_e is the electron classical radius and $y = 1/(\gamma+1)$.

The algorithm samples the energy and the direction of the delta ray and then, using this information, updates the incident particle. A rejection method provides the delta ray energy, while the azimuthal angle ϕ is generated isotropically in [0,2π] in the approximation of unpolarized particles, and finally the polar angle θ is calculated from energy-momentum conservation. The energy and direction of the incident electron or positron are then updated using the computed values.

2.2.2. Bremsstrahlung

The energy loss above the photon threshold T_γ due to the Bremsstrahlung process is simulated producing secondary photons according to the cross-section published in (Seltzer and Berger 1985). The energy-weighted cross section $S_{\mathrm{Br}}(E)$ for an electron of energy E colliding with a nucleus of charge Z, and producing a photon of energy k is given by

$$S_{\mathrm{Br}} = \frac{Z^2}{\beta_e^2} w \frac{d\sigma}{dw} \tag{14}$$

àwhere β_e is the electron relativistic velocity, and $w = k/E$. We decided to model the trend of $S_{\mathrm{Br}}(E, w)$, for a discrete set of energies from 1 keV up to 1 GeV with logarithmic steps, using a third-degree polynomial $a_0 + a_1 w + a_2 w^2 + a_3 w^3$, thus obtaining a set of coefficients $a_0(E)$, $a_1(E)$, $a_2(E)$, $a_3(E)$ as a function of the incoming electron kinetic energy E. The total cross section per atom σ_{Br} for each element is computed using

$$\sigma_{Br}(E) = \frac{\beta_e^2}{Z^2} \int_{T_\gamma}^{E} \frac{1}{w} S_{\mathrm{Br}}(w)\, dw \tag{15}$$

$$= \frac{\beta_e^2}{Z^2} \int_{T_\gamma}^{E} \frac{1}{w} (a_0(E) + a_1(E) w + a_2(E) w^2 + a_3(E) w^3)\, dw \tag{16}$$

The cross-section for each material present in the simulation, as well as the polynomial coefficients, are stored in a LUT available at run time during the kernel execution. The photon energy sampling follows the algorithm proposed by (Muhammad Abdul Wasaye and Peng 2017). The residual kinetic energy E' of the incoming electron after the Bremsstrahlung event is assumed to be $E' = E - k$, while the motion direction is obtained implying the four-momentum conservation while neglecting the nucleus momentum. The emission polar angle is sampled according to the procedure described in the PENELOPE manual (Salvat *et al* 2006), and the azimuthal angle is uniformly sampled in the range [0, 2π].

2.2.3. Photoelectric effect

In the photoelectric process, the incident photon is absorbed by a bound atomic electron followed by its ejection with kinetic energy equal to $E' = E - U_i$, where U_i is the atomic binding energy of the shell. Hence, the kinematic constraint for the minimum photon energy required for photoelectric absorption to occur is $E > U_i$. Once the target element has been selected, according to the method reported in (Schiavi *et al* 2017), the shell on which the interaction will occur is sampled. The value of the binding energy is then read from look-up tables defined from data reported in (Thompson 2001). Then, starting from the innermost shell, the first one that verifies the conditions $E > U_i$ is chosen. At this point, the energy of the emitted photo-electron is known. The polar angle θ is then sampled according to the algorithm reported in (Salvat *et al* 2006) from the differential cross section derived by (Sauter 2006):

$$\frac{d\sigma}{d\Omega} = r_e^2 \alpha^4 \left(\frac{Z}{\kappa}\right)^5 \frac{\beta^3}{\gamma} \frac{\sin^2\theta}{(1 - \beta\cos\theta)^4} \left[1 + \frac{1}{2}\gamma(\gamma - 1)(\gamma - 2)(1 - \beta\cos\theta)\right] \tag{17}$$

where r_e is the classical electron radius, α is the fine-structure constant, $\kappa = E/(m_e c^2)$, β is the ejected photoelectron Lorentz velocity and $\gamma = 1/\sqrt{1 - \beta^2}$. In our model, we have considered that the incident photon is not polarised and, hence, the angular distribution of photoelectrons is uniform in the azimuthal angle ϕ.

The emission of a photoelectron is followed by the atom de-excitation via the emission of a fluorescence photon. Such a photon has an energy equal to the difference between the binding energy of the involved shell and the next one, and it is assumed to be isotropically emitted.

2.2.4. Rayleigh scattering

In Rayleigh scattering an incident photon with energy E is scattered by bound atomic electrons. After scattering, the photon trajectory is deflected at a given polar θ and azimuthal ϕ angle. Since there is no change in the scattered photon energy, the implemented algorithm samples only θ, while ϕ is sampled uniformly in [0,2π].

The differential cross section is given approximately by (Born 1969):

$$\frac{d\sigma}{d\Omega} = r_e^2 \frac{1 + \cos^2\theta}{2} F(q, Z) \tag{18}$$

where r_e is the classical electron radius and F(q,Z) is the atomic form factor that depends only on the atomic number Z of the target element and on the momentum transfer $q = 2(E/c)\sin(\theta/2)$. The most accurate non-relativistic form factors are those reported in EPDL (Cullen *et al* 1997), which were calculated by Hubbell *et al.* (Hubbell *et al* 1975). To sample the scattering photon angle we have implemented the function F(x), used to fit the form factor F(q,Z):

$$F(x) = N(Af_1(x) + (1 - A)f_2(x)) \tag{19}$$

where N is the normalization factor, $x = q/4\pi\hbar = \sin(\theta/2)\,\mathrm{E(MeV)}\,0.8065 \cdot 10^{11}\,\mathrm{MeV^{-1}cm^{-1}}$, since $2\pi\hbar c = 1.2398 \cdot 10^{-10}$ MeV cm, and the functions $f_1(x)$ and $f_2(x)$ are:

$$f_1(x) = \frac{(1 + kx)^{-\beta}k(1 - \beta)}{(1 + k\pi)^{1-\beta} - 1} \qquad f_2(x) = \frac{2e^{-\frac{x^2}{2\sigma^2}}}{\mathrm{erf}(\frac{\pi}{\sqrt{2}\pi})\sigma\sqrt{2\pi}} \tag{20}$$

Here A, β, k and σ are the fit parameters. We have thus tabulated the four parameters for the target element with an atomic number ranging from 1 to 100 and for photon energy from 1 keV to 1 GeV, and we use them to sample the x variable and consequently the θ value. At this point, the incident photon direction is updated according to the sampled angle.

2.2.5. Compton scattering

In Compton scattering, a photon of energy E interacts with an atomic electron. As a result, the photon is scattered at an angle θ with respect to the incident direction, with a reduced energy E' and the target electron is ejected with a kinetic energy $E_e = E - E' - U_i$, where U_i is the binding energy of the involved shell. When simulating the event, it is necessary to take into account that Compton excitations are possible only if the energy transfer $(E - E')$ is larger than the binding energy of the involved shell (Binding effect) and that the atomic electrons are not at rest but move with a certain momentum distribution centered around zero (Doppler effect).

We have developed a Compton model similar to the one reported in (Böhlen *et al* 2012): to reduce the mathematical complexity of the problem, the Compton interaction is treated in the rest frame of the atomic electron. The momentum of the atomic target electron and the relative kinetic energy is sampled according to (Böhlen *et al* 2012), then we apply a Lorentz transformation in the reference frame in which the atomic electron is at rest. In this frame the scattering angle θ and the photon energy E' can be sampled from the pure Klein-Nishina differential cross section (Heitler 1936) according to the algorithm reported in (Brusa *et al* 1996):

$$\frac{d\sigma}{d\Omega} = \frac{r_e^2}{2}\left(\frac{E'}{E}\right)^2\left(\frac{E'}{E} + \frac{E}{E'} - \sin^2\theta\right) \tag{21}$$

The azimuthal angle ϕ is then sampled uniformly in [0,2π] in the approximation of unpolarized particle. The final electron momentum is obtained in the rest frame imposing four-momentum conservation. Finally, a Lorentz transformation between the reference frame where the atomic electron is at rest and the laboratory frame is applied to both the electron and photon.

2.2.6. Pair production

A photon with an energy E at least twice the electron rest energy, can be converted into an electron-positron pair in the field of an atomic nucleus or electron (with a smaller probability). For the simulation of this event we sampled the reduced energy ϵ, i.e. the fraction of the photon energy that is given to the electron, from the Bethe-Heitler differential cross section (Heitler 1936, Motz *et al* 1969, Tsai 1974), by using a rejection method (detailed in (Salvat *et al* 2006)). Once ϵ is determined the electron and positron kinetic energy are given by $E_- = \epsilon E - m_e c^2$ and $E_+ = E - E_- - 2m_e c^2$, respectively. The polar angles of the two ejected particles are sampled with the inverse-transform method of the function derived from the high-energy theory (Heitler 1936, Motz *et al* 1969):

$$p(\cos\theta_{-/+}) = N(1 - \beta_{-/+}\cos\theta_{-/+})^{-2} \tag{22}$$

where N is the normalisation constant, + and—are referred to the electron and positron respectively, and β is given by:

$$\beta_{-/+} = \frac{\sqrt{E_{-/+}(E_{-/+} + 2m_e c^2)}}{E_{-/+} + m_e c^2} \tag{23}$$

The two azimuthal angles of the two ejected particles are set to η and $\eta + \pi$, where η is sampled uniformly in the interval [0,2π].

2.2.7. Electron-positron annihilation

A positron with a kinetic energy E, penetrating a medium with an atomic number Z can annihilate *in flight* with atomic electrons. As a consequence, two photons are emitted. This process is described by the differential cross section formula of Heitler (Heitler 1936):

$$\frac{d\sigma(Z,E)}{d\epsilon} = \frac{Z\pi r_e^2}{\gamma-1}\frac{1}{\epsilon}\left[1+\frac{2\gamma}{(\gamma+1)^2}-\epsilon-\frac{1}{(\gamma+1)^2}\frac{1}{\epsilon}\right] \tag{24}$$

where $\gamma = 1 + E/m_e c^2$, with m_e electron rest mass, r_e is the classical electron radius and ϵ is the energy transferred to one of the two photons. The quantity ϵ can vary between ϵ_{min} and ϵ_{max}, corresponding to values for which photon is emitted in the opposite or in the same direction of the incident positron, respectively.

To simulate the event, the photon energy is sampled from the differential cross section and then the energy-momentum conservation is used to determine the directions of the two final photons. We have implemented the algorithm reported in (GEANT4-Collaboration 2016), which samples ϵ from equation (24) using a rejection method and then assigns to the two photons the energies ϵE and $(1-\epsilon)E$. The polar angles are obtained from energy-momentum conservation, while the azimuthal angle ϕ is uniformly generated between 0 and 2π.

The positron annihilation *at rest* is simulated every time the positron energy in the medium is lower than the cutoff T_{th}. In this case, the positron is extinguished and two photons with energy equal to the electron rest mass m_e are emitted back-to-back isotropically, neglecting the residual small non-collinearity.

3. Benchmarking and performance

To test the accuracy of FRED, photon and electron beams of 1–100 MeV have been simulated in homogeneous and heterogeneous phantoms, and the resulting dose maps have been compared to those obtained using state-of-art MCs, as FLUKA (Ferrari *et al* 2005, Battistoni *et al* 2016, Rajabi and Taherparvar 2019) and GEANT4 (Agostinelli *et al* 2003, Allison *et al* 2016, Bakkali *et al* 2018).

For the FLUKA simulations the 2020.0.10 version has been used, while for GEANT4 the *emstandard opt4* physics constructor, which has most accurate standard and low-energy models, has been chosen to obtain a higher accuracy when tracking electrons. In all the MC simulations the transport and production threshold T_{th} has been set to 50 keV for electrons/positrons and to 10 keV for photons.

A first assessment of the physical model accuracy has been achieved simulating the interaction of electron and photon beams at 1,10 and 100 MeV on water thin target (500 μm thickness). The energy and angular distribution of the secondary particles has been compared with the FLUKA predictions. The longitudinal and lateral dose distributions obtained by simulating electron and photon pencil-beams of 1, 10, and 100 MeV energy impinging on a water phantom, are also shown and compared with the results of GEANT4 and FLUKA simulations. Then the FRED performance is also presented in a more realistic case in the context of VHEE beams (70 MeV electron) on a patient CT. The results are also cross-checked against a FLUKA simulation.

To further test the accuracy of the FRED MC, an additional comparison against FLUKA simulations in the context of IORT application, is also reported.

Finally, the FRED timing performance is assessed and compared with FLUKA and GEANT4 for electron and photon pencil-beams of 1, 10 and 100 MeV impinging on a water phantom.

3.1. Test on a thin target

The test performed using a thin target allowed for the benchmarking and validation of the FRED MC against each specific physics model. The primary beam kinematic information and the one related to secondary particles generated in the target has been compared with the one computed from a FLUKA and GEANT4 simulation performed in the same conditions. The energy loss and the deflection angle at the target exit are in excellent agreement with what obtained with FLUKA and GEANT4, as can be observed in figure 2 where we show the test results at energies of 10 and 100 MeV. In particular, the FRED mean energy loss is consistent with FLUKA and GEANT4 one within 2.4% and 1.0% respectively. The same agreement, always within 5.0% and 2.5%, is also met for the mean exit angle.

The energy distribution of the delta-rays and Bremsstrahlung photons produced in the target and coming out of the target are shown in figure 3. The mean photon energy at 10 and 100 MeV obtained with FRED and the two full MCs, FLUKA and GEANT4 are in good agreement always within 2% and 0.5% respectively. While an overall good agreement can be observed between the FRED and FLUKA/GEANT4 mean photon energy (within 7% and 5% in the worst case), it is possible to clearly identify a discrepancy in the delta rays energy region close to the energy production threshold, related to the different implementations of the cut-off in the three Monte Carlo algorithms. However, as it will be shown in the next paragraph, this discrepancy in the delta-ray production has a negligible impact on the dose distributions.

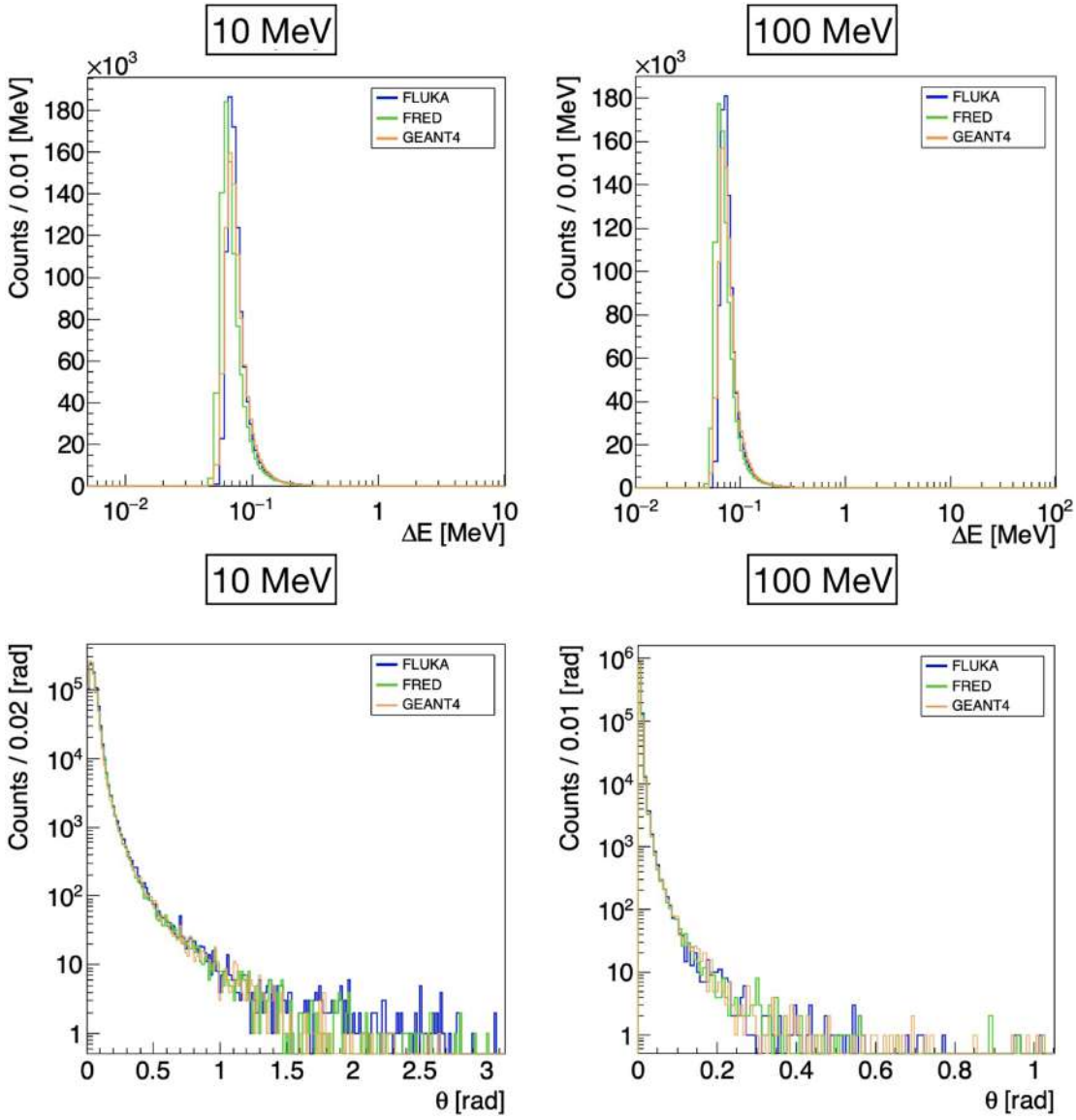

Figure 2. Comparison between FLUKA (blue), GEANT4 (orange) and FRED (green) energy loss (up) and deflection angle (down) of electron beams crossing a water target 500 μm thick.

3.2. Test on a homogeneous phantom

Figure 4 shows the depth dose distributions and lateral dose profiles at depth of maximum dose for 1, 10, and 100 MeV electron pencil-beams impinging on a homogeneous water phantom obtained using FRED, FLUKA and GEANT4. The target dimensions have been chosen depending on the particle energy: for 1 MeV electrons, a size of 1 cm $\times$ 1 cm $\times$ 1 cm was implemented with a voxel size of 0.005 cm in all the directions. For 10 and 100 MeV simulations, a water phantom of 20 cm $\times$ 20 cm $\times$ 15 cm and 20 cm $\times$ 20 cm $\times$ 50 cm with a voxel dimension of 0.05 in x and y plane and 0.1 along z was used, respectively.

In all simulations the particles entered the phantom along the z-axis after being generated in vacuum. The profiles, that represent the absorbed dose in Gy/primary, have been obtained from a simulation performed using 10^7 primary electrons to minimize the statistical fluctuations. The lateral dose profiles have been selected at the peak value of the FRED integrated depth dose distributions, i.e. at 0.16 cm, 2.60 cm and 14.0 cm for 1, 10 and 100 MeV. In the same figures, the relative dose differences are also shown. As it can be seen the agreement between the two simulations is always within 2.5%.

The same comparisons have been made also for a 1, 10 and 100 MeV photon beam with a Gaussian profile in the x and y direction with FWHM = 0.5 cm, impinging on a water phantom. Also in this case the target dimensions have been chosen depending on the particle energy: 20 $\times$ 20 $\times$ 100 cm^3 for 1 MeV, and 20 $\times$ 20 $\times$ 200 cm^3, for 10 and 100 MeV, with a voxel size of 0.05 $\times$ 0.05 $\times$ 0.5 cm^3.

Figure 5 shows the depth dose distributions and lateral dose profile obtained simulating 10^7 primary photons. Also, in this case, the photon beam travels along the z-axis in vacuum before impinging on the water

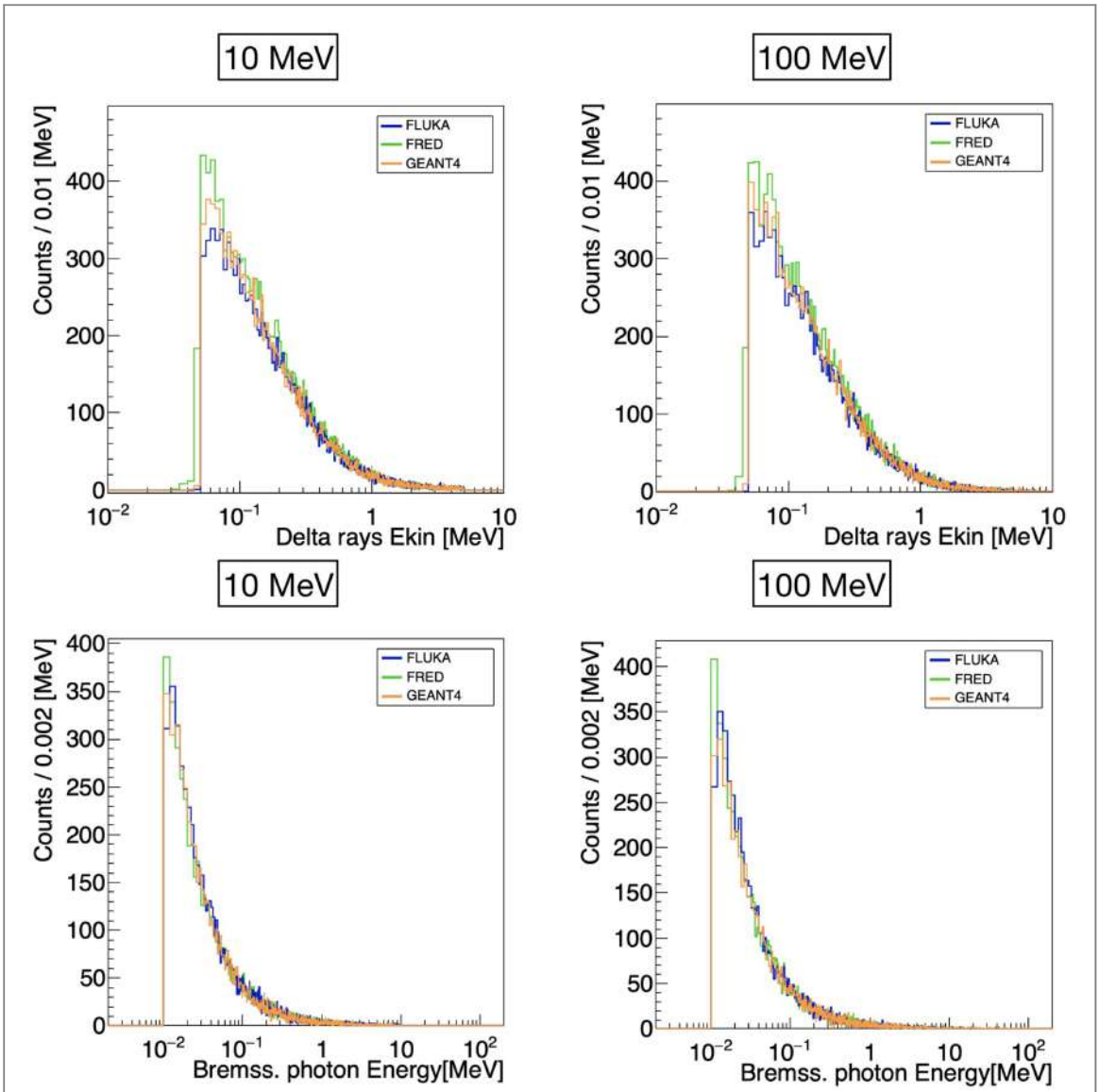

Figure 3. Kinetic energy distribution of delta-rays (up) and Bremsstrahlung photons (down) produced by electron beams at exit from the water target 500 μm thick. A small difference at energies close to production threshold, due to the different cut-off application of the three Monte Carlo codes, can be observed. FLUKA results are shown in blue line, FRED ones in green line and GEANT4 in orange line.

phantom. The lateral profiles have been selected in the fall-off region of the FRED integrated depth dose distributions, i.e. at 17 cm, 50 cm and 85 cm for 1, 10 and 100 MeV photon beam respectively. As it can be seen on the dose differences between FRED and the other two MCs shown in red, the agreement of both the longitudinal and lateral distributions is always within 2.5%.

The statistical uncertainties, identical for the three MC tools, are not graphically appreciable, being $<1\%$, and for this reason not displayed. In table 1 the FRED standard deviation of the dose value at the maximum of the electrons and photons longitudinal profiles, reported in figures 4 and 5.

3.3. Test on a non-homogeneous phantom: VHEE beams

We tested the FRED performance using as input heterogeneous materials. To this aim, we used an abdomen/pelvis and head and neck CT scans and we compared the FRED and FLUKA dose distributions.

For the former case, we simulated a 70 MeV electron field composed of 610 pencil beams with a Gaussian transverse profile of FWHM = 1 cm. Such irradiation field correspond to one of the 7 fields simulated to test the possibility of treating a real prostate cancer patient with VHEE beams (Sarti *et al* 2021). The CT has a voxel size of 1.6 mm $\times$ 1.6 mm $\times$ 2 mm respectively along the x $\times$ y $\times$ z directions. To reduce the statistical MC fluctuations to an affordable level, the simulation has been performed using 10^6 primaries for each pencil beam. Figure 6 shows the FRED and FLUKA 2D dose maps and their projection on the x, y, and z planes.

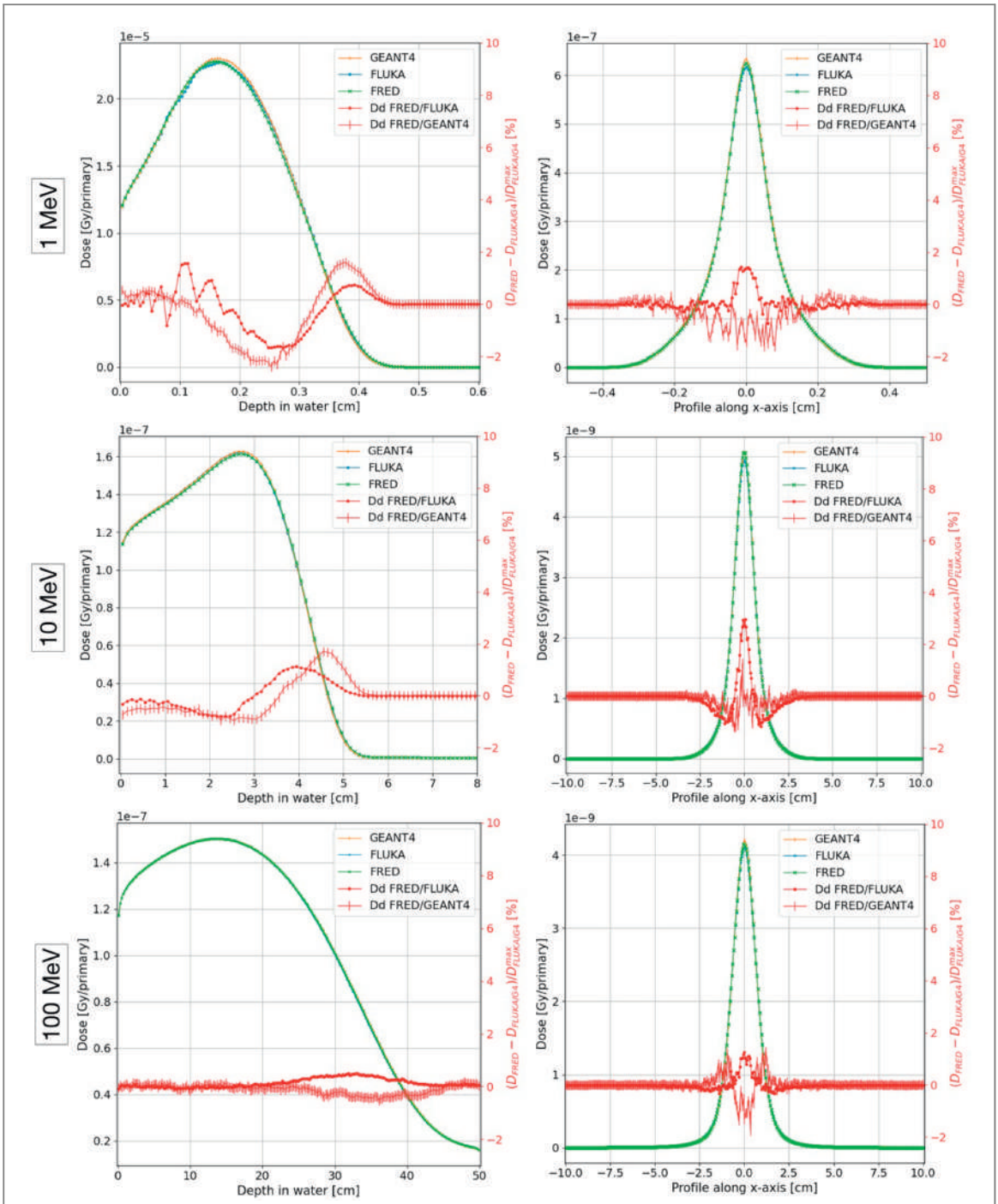

Figure 4. Longitudinal (left) and lateral (right) dose profiles for 1,10 and 100 electron pencil beams impinging on water phantom, simulated with FRED (green line), FLUKA (blue line) and GEANT4 (orange line). All the lateral profiles are evaluated at the depth for which the dose is maximum. The red curves report the dose difference (Dd) between FRED and FLUKA (dotted line) and between FRED and GEANT4 (vertical marker line). The statistical errors for the three MCs are negligible and for this reason not reported in the figures.

To test the agreement between the two distributions we have performed a 3D gamma-index analysis. The 2 mm/3 % global and local gamma-index pass rate between FRED and FLUKA dose distributions are 98.78% and 98.12%, evaluated with a threshold of 5%, with a gamma average value equal to 0.17 and 0.33 respectively.

We have then used the head and neck CT scan to evaluate the MC accuracy in a more complex situation (huge density gradient). We simulated a 110 MeV electron field composed of 386 pencil beams with a Gaussian transverse profile of FWHM = 0.5 cm. Such irradiation field corresponds to one of the three fields of a real patient treatment, treated with protons with energies ranging from 87 to 130 MeV at the Azienda Provinciale per i Servizi Sanitari (APSS). The CT has a voxel size of 0.6 mm × 0.6 mm × 1 mm respectively along the x × y × z directions. Also in this case, to reduce the statistical MC fluctuations, the simulation was performed using 10^6 primaries for each pencil beam. Figure 7 shows the FRED and FLUKA 2D dose maps and their projection on the x, y, and z planes.

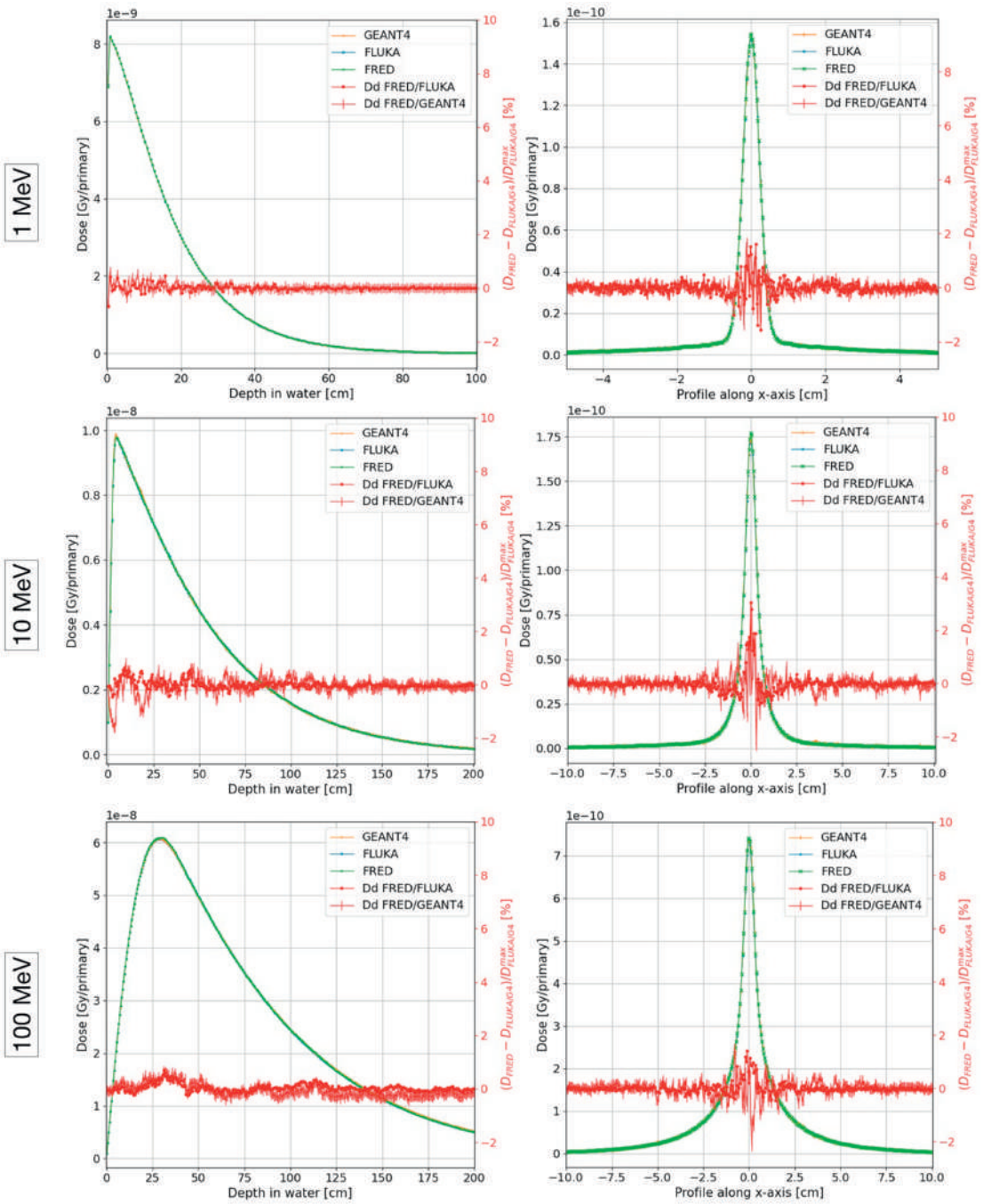

Figure 5. Absorbed dose in water for a 1,10 and 100 photon beam, with a Guassian profile (FWHM = 0.5 cm), simulated with FRED (green line), FLUKA (blue line) and GEANT4 (orange line) with the same scoring grid and the same number of primaries. On the left, it is possible to observe the absorbed dose integrated over the longitudinal axis, i.e. the beam direction. On the right, the lateral axis profile at falloff region, i.e. at 17 cm, 50 cm and 85 cm for 1, 10 and 100 MeV simulations respectively. In all the plots the red axis, on the right, reports the dose difference (Dd) between FRED and FLUKA (dotted line) and between FRED and GEANT4 (vertical marker line). The statistical errors for the three MCs are negligible and for this reason not reported in the figures.

Also in this case to asses the FRED accuracy we performed the global and local 3D gamma-index analysis with 2 mm/3 % acceptance criteria. We obtained a global and local gamma-index pass rate between FRED and FLUKA dose distributions of 99.40% and 99.28%, evaluated with a threshold of 5% of the maximum dose, with a gamma average value equal to 0.35 and 0.40 respectively.

3.4. IORT application

The implementation of the electrons interactions with matter was also tested comparing FRED and FLUKA in the context of IORT treatment when trying to reproduce the dose distribution generated by a mobile IORT linear accelerator (LINAC).

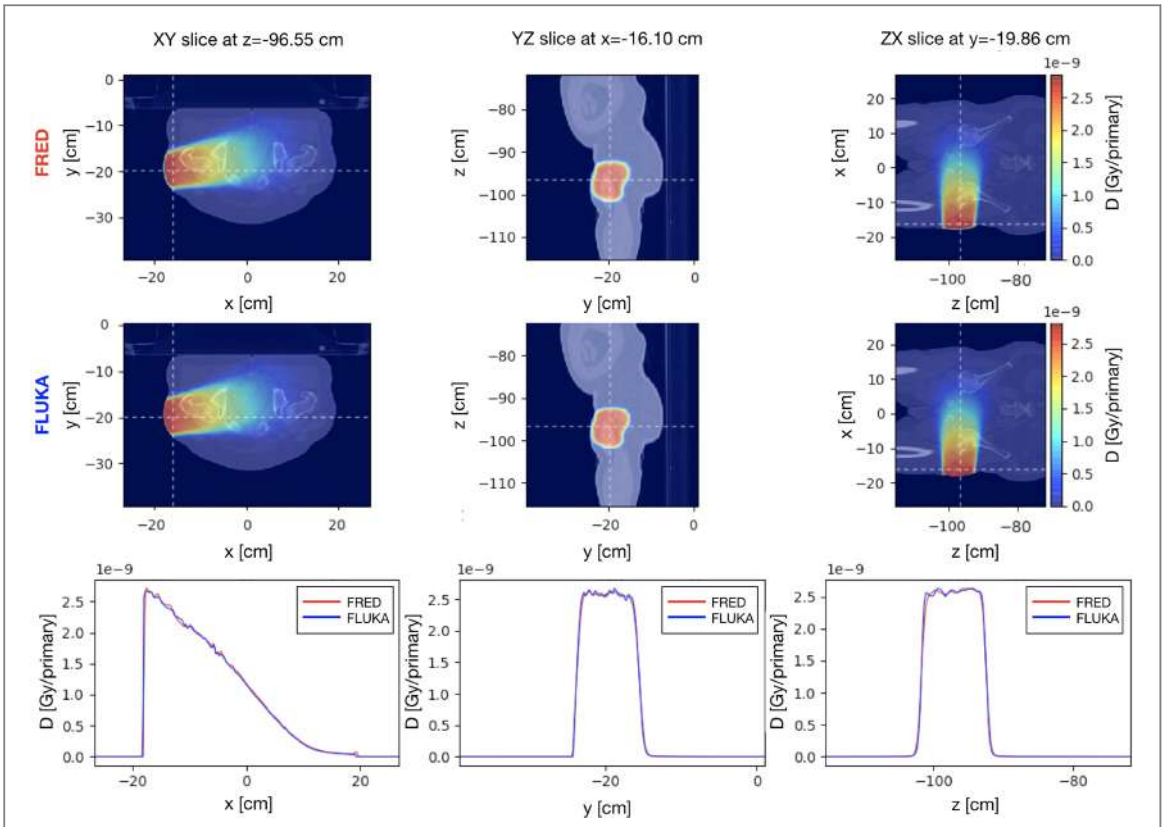

Figure 6. A comparison of the dose distributions inside the patient obtained with FRED (figures on the top and in a red line) and FLUKA (figures on the bottom and in a blue line) simulations is reported. The two first rows show the 2D dose distributions on the XY slice at z = −96.55 cm (left), YZ slice at x = −16.10 cm (center) and on the ZX slice at y = −19.86 cm (right). The projection of the 2D figures is shown on the bottom. The statistical uncertainties were not included in the plot since they are graphically inappreciable.

Table 1. Standard deviation values of the dose at the peak value of the electrons and photons longitudinal profiles. The simulations reported at 1, 10 and 100 MeV in figures 4 and 5 have been performed 10 times using 10 millions primaries.

	Statistical uncertainties		
e^- E [MeV]	σ [%]	γ E [MeV]	σ [%]
1	0.098	1	0.38
10	0.086	10	0.68
100	0.088	100	0.19

These linacs (Beddar *et al* 2006, Gunderson *et al* 2011) are typically coupled to a beam broadening system in order to target the surgical breach with a uniform irradiation. After a metallic scattering foil, a polymethylmethacrylate (PMMA) cylindrical applicator, is used, as passive collimation element, to preserve the surrounding healthy tissues from undesired radiation exposure.

The S.I.T Sordina IORT Technologies S.P.A. company[8] provided the NOVAC-11 features, i.e the applicator structure and materials crossed by the beam from the linac exit window to the applicator exit. The NOVAC-11 provides electron beams with four nominal energies, 4 MeV, 6 MeV, 8 MeV and 10 MeV, allowing to treat superficial or exposed targets with a thickness up to 2.6 cm within the 90% isodose volume.

We modelled the applicator as a series of PMMA hollow cylinders centered on the beam axis (z-axis) with different length, diameter and thickness (in the range of [3,60] mm, [20,100] mm and [5,15] mm respectively), for a total source-to-surface distance (SSD) of 80 cm. The electron beam generated by the NOVAC-11, crosses only a 60 μm thick titanium window that seals the linac vacuum chamber and, after 16 mm, four 20 μm thick steel plates, which are the ionizing chamber electrodes. In the simulation these elements have been modelled as

[8] Soiort—S.I.T. Sordina IORT Technologies S.p.A.: https://www.soiort.com

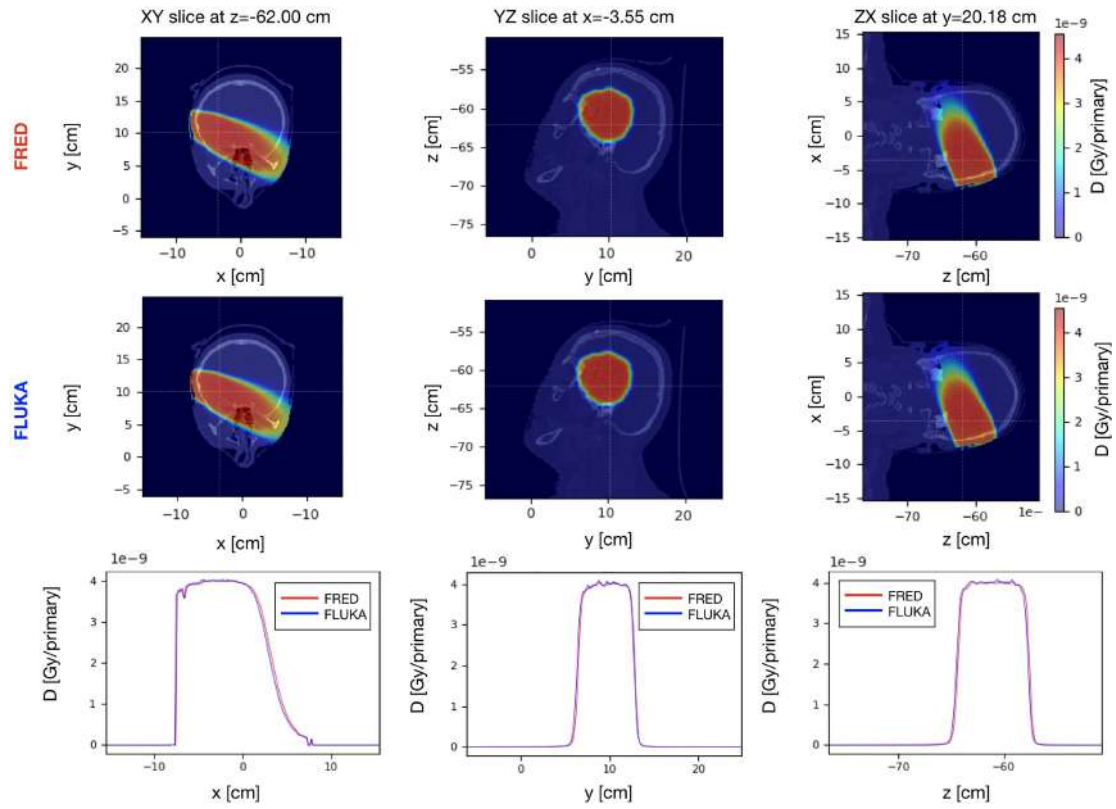

Figure 7. A comparison of the dose distributions inside the patient obtained with FRED (figures on the top and in a red line) and FLUKA (figures on the bottom and in a blue line) simulations is reported. The two first rows show the 2D dose distributions on the XY slice at z = -62.00 cm (left), YZ slice at x = -3.55 cm (center) and on the ZX slice at y = 20.18 cm (right). The projection of the 2D figures is shown on the bottom. The statistical uncertainties were not included in the plot since they are graphically inappreciable.

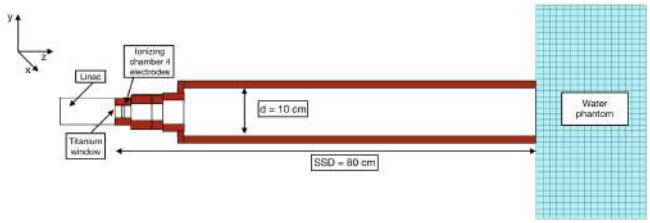

Figure 8. 2D visualization of the FRED/FLUKA simulation geometry. The beam coming out of the linac, enters the PMMA applicator region: it crosses the titanium window, four steel planes of the ionizing chamber, and impinges on a water phantom after 80 cm of air. The electron beam travels in the z direction.

disks, inserted inside the applicator, with the same dimensions and material as those supplied by the manufacturer. Figure 8 shows a 2D sketch of the simulation model.

To evaluate the dose distribution, at the end of the applicator geometry a water phantom of $40 \times 40 \times 20$ cm^3 with a voxel size of $2 \times 2 \times 1$ mm^3 has been placed.

The S.I.T company also provided the main properties of the electron beam before the titanium window: the beam has a Gaussian profile with a FWHM = 1.3 mm and a negligible mean angular spread. In this paper, we report the dose distributions obtained by simulating a mono-energetic electron beam at 10 MeV. Figure 9 shows the FRED and FLUKA 2D dose maps and their projection on the x, y and z planes. To test the agreement between the two dose distributions we have performed a gamma index analysis using 2 mm/3% acceptance criteria and 5% of threshold. The obtained global and local gamma index pass rate is 99.80% and 99.67% with a gamma average equal to 0.16 and 0.22 respectively.

3.5. Efficiency and timing performance

The FRED package couples an accuracy comparable with that one of state-of-the-art MC software with an outstanding timing performance.

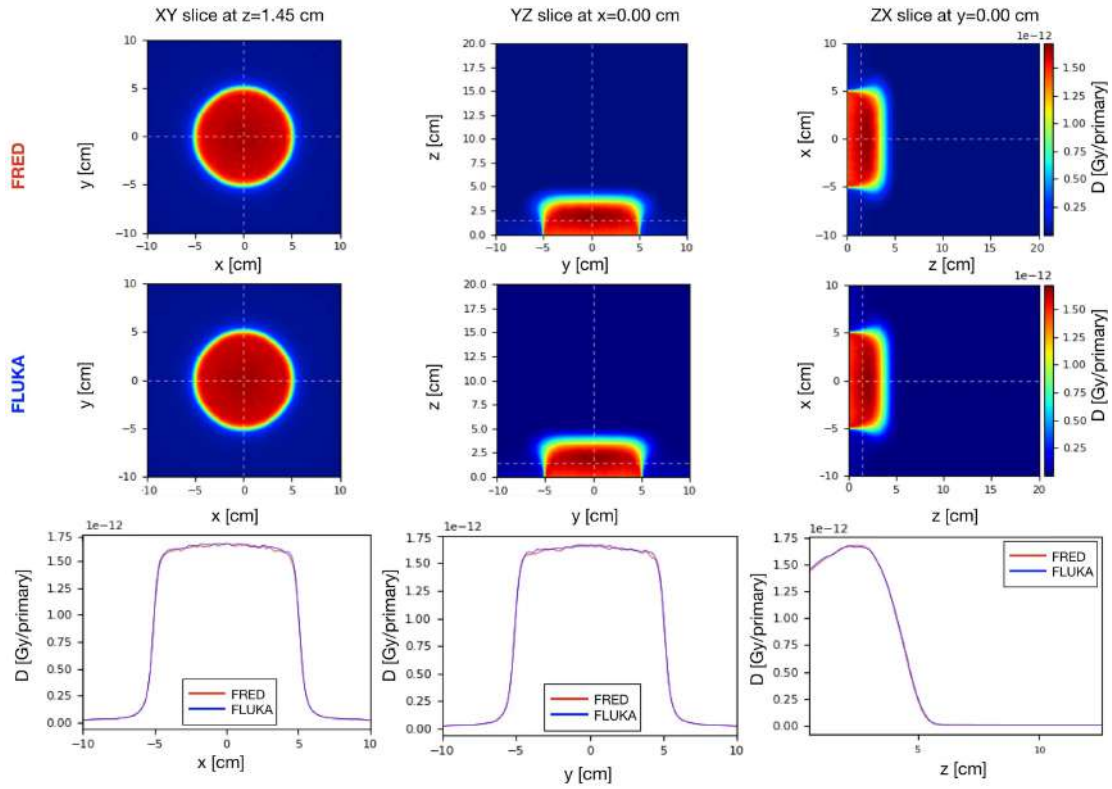

Figure 9. Comparison of the dose distributions inside the water phantom obtained with FRED (figures on the top and in a red line) and FLUKA (figures on the bottom and in a blue line) simulations of a IORT LINAC To reduce the statistical MC fluctuations both simulations have been performed using 10^8 10 MeV primary electrons. The two first rows show the 2D dose distributions on the XY slice at z = 1.45 cm (left), YZ slice at x = 0.00 cm (center) and on the ZX slice at y = 0.00 cm (right). The projection of the 2D figures, superimposed, is shown on the bottom. The statistical uncertainties were not included in the plot since they are graphically inappreciable.

Table 2. Timing performance obtained simulating 1,10 and 100 MeV electron and photon beam impinging respectively on a water phantom of $20 \times 20 \times 20\, cm^3$ with a 0.2 cm cubic voxels, and $20 \times 20 \times 500$ with a $0.2 \times 0.2 \times 1$ cm^3 voxel size, for two state-of-art full MCs (FLUKA and GEANT4 running on Intel(R) Core(TM) i5-10400 CPU) and for FRED running on NVIDIA Geforce RTX 3090 GPU. The tracking rate is reported in primary/s. The FRED efficiency with respect to the FLUKA and GEANT4 one is also reported. In the last column, the standard deviation of the dose at the maximum value of the longitudinal profiles, for electrons, and at the falloff region for photons is shown.

	Tracking rate and efficiency					
Simulation setup	T_{FLUKA} [prim/s]	T_{GEANT4} [prim/s]	T_{FRED} [prim/s]	$\frac{\epsilon_{FRED}}{\epsilon_{FLUKA}}$	$\frac{\epsilon_{FRED}}{\epsilon_{GEANT4}}$	σ [%]
e^- @ 1 MeV	$1.6 \cdot 10^4$	$1.3 \cdot 10^3$	$3.0 \cdot 10^6$	190	2300	0.037
e^- @ 10 MeV	$4.4 \cdot 10^3$	$2.2 \cdot 10^2$	$4.0 \cdot 10^5$	90	1800	0.065
e^- @ 100 MeV	$1.1 \cdot 10^3$	$4.8 \cdot 10^1$	$7.2 \cdot 10^4$	70	1500	0.054
γ^- @1 MeV	$1.6 \cdot 10^4$	$1.6 \cdot 10^4$	$7.5 \cdot 10^5$	50	50	0.316
γ^- @ 10 MeV	$4.3 \cdot 10^3$	$3 \cdot 10^3$	$1.7 \cdot 10^5$	40	60	0.531
γ^- @ 100 MeV	$5.4 \cdot 10^2$	$3.2 \cdot 10^2$	$1.9 \cdot 10^4$	40	60	0.143

In table 2, the FRED, FLUKA and GEANT4 computing time for different simulations are reported in primary/s units. For this analysis, an electron and photon pencil beams of 1, 10, and 100 MeV energies impinging on a water phantom (20 cm × 20 cm × 20 cm with a 0.2 cm cubic voxels for electrons and 20 cm × 20 cm × 500 cm with 0.2 × 0.2 × 1 cm voxel size for photons) have been simulated.

In the same table, the FRED efficiency is also reported. The MC simulation efficiency $\epsilon = 1/(\sigma^2 T)$ is inversely proportional to the simulation variance σ^2 and the time calculation T required to obtain this variance (Chetty *et al* 2007). To evaluate and compare the FRED efficiency we considered the simulations performed on the

homogeneous water phantoms with electrons and photons beam at 1, 10 and 100MeV, reported in table 2. For each simulation setup, we computed the standard deviation σ of the maximum dose value of the longitudinal dose profiles on 10 independent FRED, FLUKA and GEANT4 simulations. Since the statistical uncertainties in all the simulations were identical, the efficiency comparisons are therefore equivalent to the calculation time ones. Table 2 shows the $\epsilon_{FLUKA}/\epsilon_{FRED}$ and $\epsilon_{GEANT4}/\epsilon_{FRED}$ obtained from the ratio of the MC total simulation times per 1 million electrons and photons transported.

As shown, profiting from both the simplification of the implemented physics models and the parallel computing power of GPU architectures (NVIDIA Geforce RTX 3090), FRED is capable to reduce the simulation time by a factor of ~1000 and ~5000, depending on the beam energy, when comparing with FLUKA and GEANT4 full MC results respectively (running on a single CPU core of an Intel(R) Core(TM) i5-10400 CPU).

As expected, the timing performance decreases with increasing beam energy, since electrons or photons with higher energies are subject to more interactions, their average path through the medium is longer and thus the number of produced secondary particles is also higher. As an example, for an electron beam of 1, 10 and 100 MeV energies crossing a $20 \times 20 \times 20$ water phantom, the average number of secondary particles per primary is 0.84, 12.7 and 61.2 respectively using an energy cutoff equal to 50 keV for electrons and positrons and 10 keV for the photons.

We have also tested the FRED timing performance against other fast MC GPU-based, as goMC (Tian *et al* 2015). According to (Tian *et al* 2015), we simulated a 2×2 cm^2 electron beam at 15MeV impinging on on s $32 \times 32 \times 32$ water phantom with a voxel size of 0.25 cm^3. By choosing the same production and transport energy threshold, i.e. 200 keV for electrons and 50 keV for photons, we obtained comparable results in terms of computational time.

4. Conclusions

In this work we presented a fast MC software focused to radiotherapy applications capable of reproducing dose distributions in homogeneous and heterogeneous phantoms with an accuracy at the level of state-of-art full MCs and with an impressive gain in processing time.

The electromagnetic interactions have been simulated choosing the best physical models in literature, such as the ones used by GEANT4 or PENELOPE, and simplifying their algorithm to reduce as much as possible the simulation time with no loss in accuracy.

When comparing FRED dose maps with FLUKA or GEANT4 the relative dose difference between the longitudinal and lateral dose profiles obtained propagating both electron and photon beam in a water phantom is always within 2.5% in the 1–100 MeV energy range. Simulating also a field of a prostate cancer radiotherapy treatment with VHEE using as input an abdomen/pelvis CT scan, we have obtained a very good pass rate for 2 mm/3% gamma-index comparing FRED and FLUKA dose maps. The same result has been obtained also when exploring the IORT applications: using FRED and FLUKA we simulated in detail the NOVAC 11 IORT applicator and we compared the dose distribution at the exit of the applicator in a water phantom obtaining an almost 100% gamma index pass rate.

The observed gain in processing time when comparing FRED to state-of-art full MCs, running on CPU, is impressive: FRED shows a factor of ~1000 or ~5000 with respect to FLUKA and GEANT4 respectively, depending on the particle type and energy. Comparing the time performance of FRED with the other GPU MCs, such as goMC (GPU OpenCL Monte Carlo) (Tian *et al* 2015) recently developed for external photon and electron radiotherapy in the MeV energy range, we observed consistent results in terms of timing performance and accuracy.

A straightforward application of the FRED software can be the recent developments in electron beam therapy, i.e. VHEE beams for deep seated tumour treatment, and the increasing interest in the IORT technique, that may represent one of the first clinical implementation of a FLASH treatment. In this realm the FRED Monte Carlo could provide a complete treatment plan or be used for the dose recalculation achieving a clinical precision within minutes instead of days, exploiting the scalable parallel computing power of the GPU architecture.

Appendix: Tabulated databases

Table 3. The table summarizes the tabulated quantities for each implemented process. Some of them have been directly downloaded from available database, e.g. the NIST, while others are computed at the simulation initialisation according to the implemented algorithm

	Tabulated database	
Process	Source	Tabulated quantities
Mean energy loss	NIST	Unrestricted Stopping power
Energy straggling	GEANT4	$\bar{n}_1$, $\bar{n}_2$, $\bar{n}_{ion}$ and $\Delta E_{ion}(\bar{n}_{ion}, T_{th})$
Multiple scattering	Al-Beteri	X_c, B and F(Z,t)
Möller and Bhabha scattering	GEANT4	Cross section
Bremsstrahlung	NIST	Cross section
	Custom code	a_0, a_1, a_2 and a_3
Photoelectric effect	NIST	Cross section
	Custom code	Binding Energies
Rayleigh Scattering	NIST	Cross section
	Custom code	A, β, k and σ
Compton effect	NIST	Cross section
	Custom code	Momentum p of the atomic electron
Pair Production	NIST	Cross section
Electron-Positron annihilation	NIST	Cross section

ORCID iDs

G Franciosini https://orcid.org/0000-0001-8088-953X
M Marafini https://orcid.org/0000-0003-1282-0383
A Sarti https://orcid.org/0000-0001-5419-7951

References

Agostinelli S *et al* 2003 GEANT4-a simulation toolkit *Nucl. Instrum. Meth.* A **506** 250–303
Al-Beteri A A and Raeside D E 1988 An improved electron multiple-scattering distribution for monte carlo transport simulation *Med. Phys.* **15** 351–7
Allison J *et al* 2016 Recent developments in geant4 *Nucl. Instrum. Methods Phys. Res., Sect. A* **835** 186–225
Battistoni G *et al* 2016 The fluka code: An accurate simulation tool for particle therapy *Frontiers in Oncology* **6** 116
Beddar A S *et al* 2006 Intraoperative radiation therapy using mobile electron linear accelerators: Report of aapm radiation therapy committee task group no. 72 *Med. Phys.* **33** 1476–89
Berger J 1963 *Monte Carlo Calculation of The Penetration and Diffusion of Fast Charged Particles Methods in Computational Physics New York* vol 1 (New York: Academic) pp 135–215
Berger M J and Seltzer S M 1982 Stopping powers and ranges of electrons and positrons *US. Nat. Bureau Stand. Inst. Basic Stand.* (Washington, DC)
Böhlen T T, Ferrari A, Patera V and Sala P R 2012 Describing compton scattering and two-quanta positron annihilation based on compton profiles: two models suited for the monte carlo method *J. Instrum.* **7** P07018
Born M 1969 *Atomic Physics* (London: Blackie & Son)
Brusa D *et al* 1996 Fast sampling algorithm for the simulation of photon compton scattering *Nucl. Instrum. Methods Phys. Res., Sect. A* **379** 167–75
Butcher J 1996 A history of runge-kutta methods *Appl. Numer. Math.* **20** 247–60
Chetty I J *et al* 2007 Report of the aapm task group no. 105: Issues associated with clinical implementation of monte carlo-based photon and electron external beam treatment planning *Med. Phys.* **34** 4818–53
Cullen D E, Hubbell J H and Kissel L 1997 *Epdl97: the evaluated photo data library 97 version*UCRL-50400-Vol.6-Rev.5 (https://doi.org/10.2172/295438)
De Simoni M *et al* 2022 A data-driven fragmentation model for carbon therapy gpu-accelerated monte-carlo dose recalculation *Frontiers in Oncology* **12** 169–84
Diffenderfer E S *et al* 2020 Design, implementation, and in vivo validation of a novel proton flash radiation therapy system *International Journal of Radiation Oncology*Biology*Physics* **106** 440–8
EL Bakkali J, Doudouh A and Mansouri H 2018 Assessment of monte carlo geant4 capabilities in prediction of photon beam dose distribution in a heterogeneous medium *Physics in Medicine* **5** 1–5
Faillace L *et al* 2021 Compact s-band linear accelerator system for ultrafast, ultrahigh dose-rate radiotherapy *Phys. Rev. Accel. Beams* **24** 050102
Favaudon V *et al* 2014 Ultrahigh dose-rate flash irradiation increases the differential response between normal and tumor tissue in mice *Sci. Transl. Med.* **6** 245ra93–245ra93
Ferrari A *et al* 2005 *FLUKA: A multi-particle transport code (Program version 2005)*CERN-2005-010, SLAC-R-773, INFN-TC-05-11
GEANT4-Collaboration 2016 *Physics Reference Manual*
Grassberger C, Lomax A and Paganetti H 2014 Characterizing a proton beam scanning system for monte carlo dose calculation in patients *Phys. Med. Biol.* **60** 633–45
Gunderson L *et al* 2011 *Intraoperative Irradiation: Techniques and Results* (New Jersey: Humana Press)
Heitler W 1936 The quantum theory of radiation *International Series of Monographs on Physics* vol 5 (Oxford: Oxford University Press)
Hubbell J H *et al* 1975 Atomic form factors, incoherent scattering functions, and photon scattering cross sections *J. Phys. Chem. Ref. Data* **4** 471–538
Jia X *et al* 2014 GPU-based high-performance computing for radiation therapy *Phys. Med. Biol.* **59** R151–82
Karbalaee M *et al* 2020 A novel gpu-based fast monte carlo photon dose calculating method for accurate radiotherapy treatment planning *Journal of Biomedical Physics and Engineering* **10** 329–40
Liang Y *et al* 2020 A general-purpose monte carlo particle transport code based on inverse transform sampling for radiotherapy dose calculation *Sci. Rep.* **10** 9808
Marsaglia G and Zaman A 2006 The kiss generator *Technical Report, Department of Statistics, Florida State University, Tallahassee, FL, USA.*
Mein S *et al* 2018 Fast robust dose calculation on gpu for high-precision 1h, 4he, 12c and 16o ion therapy: the frog platform *Sci. Rep.* **8** 14829
Men C *et al* 2009 GPU-based ultrafast IMRT plan optimization *Phys. Med. Biol.* **54** 6565–73
Montay-Gruel *et al* 2021 Flash radiotherapy with photon beams *Medical Physics* **49** 2055– 67
Motz J W *et al* 1969 Pair production by photons *Rev. Mod. Phys.* **41** 581–639
Muhammad Abdul Wasaye W H and Peng H 2017 An algorithm for monte carlo simulation of bremsstrahlung emission by electrons *Nucl. Sci. Tech.* **28** 71
National Institute of Standards and Technology 2002 Security requirements for cryptographic modules *Technical Report Federal Information Processing Standards Publications (FIPS PUBS) 140-2, Change Notice 2 December 03, 2002* (Washington, D.C.: U.S. Department of Commerce)
NVIDIA, Vingelmann P and Fitzek F H 2020 'Cuda, release: 10.2.89'
Paganetti H 2009 Dose to water versus dose to medium in proton beam therapy *Phys. Med. Biol.* **54** 4399–421
Rajabi R and Taherparvar P 2019 Monte carlo dosimetry for a new 32p brachytherapy source using fluka code *Journal of Contemporary Brachytherapy* **11** 76–90
Ronga M G *et al* 2021 Back to the future: very high-energy electrons (vhees) and their potential application in radiation therapy *Cancers* **13** 19
Salvat F *et al* 2006 A code system for monte carlo simulation of electron and photon transport *Workshop Proceedings, Data Bank NEA/NSC/DOC(2011)5, Barcelona*
Sarti A *et al* 2021 Deep seated tumour treatments with electrons of high energy delivered at flash rates: the example of prostate cancer *Frontiers in Oncology* **11** 5209

Sauter F 2006 Über den atomaren photoeffekt in der k-schale nach der relativistischen wellenmechanik diracs *Ann. Phys.* **403** 454–88
Schiavi A *et al* 2017 Fred: a GPU-accelerated fast-monte carlo code for rapid treatment plan recalculation in ion beam therapy *Phys. Med. Biol.* **62** 7482–504
Seltzer S M and Berger M J 1985 Bremsstrahlung spectra from electron interactions with screened atomic nuclei and orbital electrons *Nucl. Instrum. Methods Phys. Res., Sect. B* **12** 95–134
Thompson A 2001 *X-ray Data Booklet Lawrence Berkeley National Laboratory* (California: University of California)
Tian Z *et al* 2015 A GPU OpenCL based cross-platform monte carlo dose calculation engine (goMC) *Phys. Med. Biol.* **60** 7419–35
Tsai Y S 1974 Pair production and bremsstrahlung of charged leptons *Rev. Mod. Phys.* **46** 815–51
Wan Chan Tseung H *et al* 2015 A fast gpu-based monte carlo simulation of proton transport with detailed modeling of nonelastic interactions *Med. Phys.* **42** 2967–78
Wang Y *et al* 2016 A gpu-accelerated monte carlo dose calculation platform and its application toward validating an mri-guided radiation therapy beam model *Med. Phys.* **43** 4040–52